Insights into core-mantle differentiation from bulk Earth melt simulations

Abin Shakya[1], Dipta B Ghosh[1], Colin Jackson[2], Gabriele Morra[3] & Bijaya B Karki[1,*]

[1]School of Electrical Engineering and Computer Science, Department of Geology and Geophysics, Center for Computation and Technology, Louisiana State University, Baton Rouge, LA 70803, USA

[2]Department of Earth and Environmental Sciences, Tulane University

[3]Department of Physics, University of Louisiana at Lafayette

[*]Corresponding author: bbkarki@lsu.edu (B.B. Karki)

The earth is thought to have gone through complex physicochemical changes during the accretion and magma ocean stages. To better understand this evolution process at the fundamental level, we investigate the behavior of a bulk earth melt system by simulating the composition $Fe_{35.7}Mg_{19.0}Si_{15.2}O_{30.2}$ (in wt%) at high pressure. A deep neural network potential trained by first-principles data can enable accurate molecular dynamics simulation of large supercells that greatly enhances sampling and offers reliable evaluation of elemental partitioning. Our simulated system undergoes a phase separation in which the four elements clump together to different extents into two major domains. Based on the coordination and space-decomposition analyses, the inferred composition at 3000 K and 29.1 GPa contains 96.2, 0.1, 1.9 and 1.7 wt% of Fe, Mg, Si, and O, respectively, for the one domain and the corresponding elemental proportions are 3.0, 29.7, 22.0, and 45.3 wt% for the other domain. The predicted segregation thus leads to the formation of an iron-rich phase which corresponds to the metallic core and a magma ocean phase which corresponds to the silicate mantle. The metallic domain incorporates more silicon and more oxygen whereas the magma ocean domain gains more iron oxides at higher temperatures. Our predicted compositions compare favorably with those derived from experimental work for the equilibrium state melt and silicate reacting under high-pressure conditions.

During the accretion process, various materials including metals, silicates, and volatiles were gradually accumulated to form the planetesimals and protoplanets which were eventually added to the growing planets, including the earth. The early earth is believed to have been frequently in a molten state primarily because of repeated high-energy impacts by the planetesimals and meteorites. The molten state might have persisted to different extents, including magma ocean stage until the formation of the core completed[1,2]. As such, the compositions of melts then are expected to approach the bulk composition of the earth, and we can assume that our planet was a mixed metallic liquid-magma ocean system. It is of fundamental importance to understand the physical/dynamical and chemical behavior of a molten bulk earth system at the pressure-temperature conditions that are relevant to the core formation. A critical stage in the accretion and magma ocean processes was the chemical differentiation of metal from silicate that eventually led to the formation of a metallic core and of a silicate mantle[3,4]. It is generally believed that this differentiation process took place during the early history of all terrestrial planets.

The present-day compositions of the earth's core and mantle critically depend on the extent and nature of metal-silicate equilibration. All elements partitioned to different extents between the segregated core-forming metallic liquid and mantle-forming silicate magma ocean. Therefore, both the metal-silicate differentiation and element partitioning have been studied extensively[5-7]. The aim is to gain insight into the processes that occurred during the planetary accretion and the role that metal-silicate differentiation plays in the formation of planetary interiors. Observational approaches involve analyzing the meteorites and planetary samples to understand their composition[8,9]. Experimental methods can be designed to synthesize materials representative of natural samples undergoing the differentiation. For instance, the analysis of such samples suggests that early metal-silicate differentiation can occur through the percolation of an interconnected metallic network thus allowing an efficient separation[10,11]. This implies that the complete differentiation occurs for bodies accreted earlier than that experienced a magma ocean stage. Measurements of the metal-silicate partitioning coefficients of siderophile elements, as well as the mantle concentrations of siderophile elements, suggest that early-forming cores continued to react with progressively deeper magma oceans as accretion progressed[12,13]. It is in this higher temperature and pressure stage of metal-silicate reactions where it is believed that common light elements, including Si and O, become soluble in core-forming metal, ultimately yielding the modern chemistry of the core that is demonstrably less dense than a pure Fe-Ni alloy[14]. These higher pressure and temperature conditions are challenging to experimentally simulate and meteorites only provide direct evidence for metal-silicate reactions under relatively mild-pressure temperature conditions.

Molecular dynamics simulations allow us to understand the microscopic (atomic) scale of a molten earth during the accretion and magma ocean periods over a wide range of pressure-temperature space. Because of their complex and computation-intensive nature, such simulations pose tremendous challenges. The commonly used pair potentials molecular dynamics approach

generally does not work for iron-bearing systems whereas accurate first-principles approach is computationally intensive, limiting the size and duration of simulations. Nevertheless, first-principles-based studies made pioneering efforts to simulate bulk earth-like systems with liquid iron and silicate melt phases and yield estimates for equilibrium composition of each phase, including the metal-silicate partitioning of volatile elements[15,16]. These studies faced challenges related to the small supercells simulated and the computational geometry techniques used for the data analysis. It is inherently more difficult to quantify the composition of a phase as the number of atoms associated with that phase decreases. These challenges can be mitigated if a sufficiently large supercell is simulated and the distributions of atoms within the supercell are carefully analyzed using the atomic position-time series data.

Here we report a combined molecular dynamics study of a bulk earth-like melt system using the firs-principles approach[17] and deep neural network-based potential[18]. Lately, the use of deep potentials trained with the first-principles data is increasing in the study of complex materials problems of geophysical and geochemical importance[19-22]. The supercells containing four major elements Fe, Mg, Si, and O in the proportions which are comparable to the bulk earth composition[23] are simulated at the pressure-temperature-redox conditions (29 to 35 GPa, 3000 to 4000 K, and IW–3 to IW–2) relevant to the planetary accretion and magma ocean stages[24]. These conditions also permit direct comparison of simulation results with experimental inferences. The starting configuration is a random distribution of three cations which are locally coordinated/bonded with anions to similar extents (Supplementary Fig. S1). This serves as a well-mixed system of metallic liquid and silicate representative of the magma ocean. During the molecular dynamics simulation, the constituent atoms move around, and the system eventually approaches equilibration with two different liquid configurations. We analyze the atomic-position time series (snapshots) using the pair-correlation and space-decomposition techniques to confirm that the melt system undergoes the anticipated metal-silicate differentiation. These techniques allow us to accurately characterize the segregated liquid phases corresponding to iron-rich metallic and iron-poor silicate regions to infer their respective compositions. Finally, we discuss the implications of our results for the composition of the core and mantle of the present Earth.

Results and analysis

We start by considering the atomic visualization snapshots of the initial and equilibrated configurations for the 512-atom supercell used in the FPMD simulation (Fig. 1, top). In the initial snapshot, Fe, Mg, and Si are distributed randomly each being surrounded by oxygen atoms to similar extent, that is, all three cations are well bonded with oxygen. During the simulation, the constituent atoms have moved around considerably thus resulting in a different arrangement. In particular, the iron atoms tend to clump together, and the other atoms seem to have responded to this clustering activity. The rearrangement of the atoms implies a possible separation of the melt into two or more phases, and such phase segregation becomes visually more pronounced for the large-supercell configuration obtained from the DPMD simulation (Fig. 1, bottom). We examine

the structural and chemical behavior of the simulated bulk earth melt system by analyzing and visualizing the atomic position-time series data. First, we present the calculated radial distribution functions and coordination environments to understand the atomic correlations and local structures. Second, we perform space decomposition of the supercell to explore the spatial distributions of different elements at the sub-region or cell level. This helps us accurately mark the segregated phases if they exist. After establishing the spatial extent of the segregated phases, we infer their compositions by the counting the different elements that are present in each phase. Our analysis first focuses on the FPMD simulation and then compares the findings with those based on the large and long DPMD simulations at 3000 K and 29.1 GPa and at higher temperatures.

RDF and coordination. The simulated melt system shows ten types of atomic pair-wise correlations. A clear and atypically shaped peak exists in the radial distribution functions of Fe, Mg, and Si defined with respect to O (Fig. 2, left). The peak amplitude differs considerably among them though these cations are present in similar numbers in the supercell. Particularly, the Fe-O peak is much shorter than the Mg-O and Si-O peaks with its maximum located between them (at distance of 1.83 Å). Among all like- and unlike-cation pair correlations (Fig. 2, right), the Fe-Fe RDF shows the strongest peak which is located at the shortest distance of 2.25 Å followed by a noticeable second peak. The Fe-Si RDF shows a shorter peak also around this location, which is not far from the Fe-O peak position. In contrast, the Fe-Mg RDF has a broad peak with a maximum value being lower than the one and the two cations thus tend to avoid each other. All Mg/Si-Mg/Si functions show a clear peak located at larger distances around 3 Å and manifest similar correlations as in silicate liquids. Based on our comparison of all pair correlation functions that exist in the simulated bulk earth melt system, Fe behaves differently than the other two cations in that it is strongly self-correlated but weakly correlated with O.

The partial radial distribution functions from the FPMD simulation almost overlap with those from the DPMD simulation using the 512-atom supercell (Supplementary Fig. S2). However, we find that the partial RDFs using the large 32768-atom supercell configurations from the DPMD simulation show notable differences from the FPMD results. The Fe-Fe peak gets taller whereas the Fe-O, Fe-Mg, and Fe-Si peaks all become shallower for the large supercell (Fig. 2). As more Fe atoms can afford to gather in the large system compared to the small system, they tend to avoid other elements. This enhanced clustering activity is also manifested with the anomaly that Fe-Fe and other iron-involved functions deviate from unity at long distances (Supplementary Fig. S3). All correlation functions involving Mg, Si, and O remain essentially unchanged between the small and large systems and they also approach unity at long distances.

To gain further insight into the local structure around Fe atoms, we examine all its coordination types in comparison with the coordination environments of other two cations (Fig. 3, Supplementary Fig. S2). At 3000 K and 29.1 GPa, the calculated mean Fe-O coordination number (Z_{FeO}) is ~1.5, which is much smaller than the Mg-O and Si-O coordination numbers of 6.5 and

4.2, respectively. Z_{FeO} takes even smaller value of 0.75 for the large supercell. However, Z_{FeO} is close to 5 for iron-bearing melts[25,26], such as $Fe_{0.25}Mg_{0.75}O$ and $Fe_{0.25}Mg_{0.75}SiO_3$. It is thus apparent that the Fe-O bonding is largely suppressed in the bulk earth melt compared to normal silicate and oxide melts and correspondingly, the FeO coordination distribution is dominated by uncoordinated states and singly and doubly coordinated states (Fig. 3). On the other hand, the Mg-O coordination exhibits atypically shaped distribution and almost entirely represents polyhedral MgO_n groups with $n \geq 4$ (Fig. 3). Such structural motifs are also present in high abundance (>75%) for the Si-O coordination but in much smaller abundance (< 10%) for the Fe-O coordination. These coordination polyhedra can be considered to mimic the local surroundings of cations typically found in molten oxides and silicates whereas the undercoordinated Mg/Fe/Si-O states likely belong to Fe-rich areas.

The Fe-Fe coordination has a mean value of 8.1 and shows a rather broad distribution for the small system, and the distribution considerably shifts to the right taking a higher mean value of 10.9 for the large system (Fig. 3, Supplementary Fig. S4). Nine-fold and higher coordination species present in significant abundances correspond to a region which is enriched in Fe atoms. On the other hand, the undercoordinated species, particularly isolated and singly coordinated atoms present in small abundances perhaps represent Fe-depleted areas. It is also interesting to note that Fe is directly bonded with Si to significant extent as indicated by a clear Fe-Si RDF peak (Fig. 2, right). The corresponding mean coordination numbers Z_{FeSi} and Z_{SiFe} are 1.6 and 1.9, respectively, for the small system and 0.71 and 0.84, respectively, for the large system. A small fraction of Si is coordinated with nine or more Fe atoms, apparently belonging to Fe-rich areas.

To visualize the melt structure in terms of the atomic coordination/bonding environments[27], we draw bonds/links between the atoms in each pair that falls within the first peak of the corresponding radial distribution function and in the case of high coordination states, we use the polyhedral representation. As can be seen in the visualization snapshots (Fig. 4, top-left), all Fe atoms are linked with each other thereby forming an easily identifiable cluster. The Fe atoms are not bonded with oxygen in the central part of the cluster and tend to bond more with O in the outer part (Fig. 4, top-right). We can see the Fe-O coordination polyhedra away from the cluster in the case of the large supercell configuration (Fig. 4, bottom). The surrounding region contains Mg/Si-O polyhedral units which are absent within the cluster (Supplementary Fig. S5). Undercoordinated states in which the Si or Fe atom is bonded with two or three O atoms appear to separate the cluster from the surrounding Fe-depleted region. This separation becomes more evident in the large system (Fig. 4, bottom).

Space decomposition. Based on the local coordination and bonding environments of Fe and other elements, the constituent atoms of the simulated melt system are not distributed homogeneously within the supercell. To further understand the spatial distribution of four elements qualitatively and quantitatively, we analyze the atomic position-time series data by performing space

decomposition (Supplementary Fig. S6). The 512-atom supercell of length of 17.0 Å is divided into the 4×4×4 mesh, resulting in 64 cubic cells each of which on average contains 8 atoms. For a given snapshot, we count the number of different elements separately in each cell. This is essentially doing a three-dimensional binning in which the cubic cell serves as a bin. The per-cell atom count (n) is expected to vary between 0 when a given element does not exist in the cell and 8 when the same element completely fills up the cell. If the cell is more than half-filled with a given atomic species, we have $n > 4$. A given value of n can be found for multiple cells, so we calculate the frequency of its occurrence (f) by counting the cells (bins) which contain the same number of the element under consideration. The cell occupancy frequency distributions are then averaged over the entire simulation steps for each element.

Fig. 5 (left) shows the cell occupancy frequency for each of four elements as a function of the per-cell atom count (n) for the FPMD position-time series at 3000 K. The Fe-cell frequency distribution has the highest value for the zero-atom cell and decreases rapidly initially and then more gradually for higher atom counts. More than half of the cells (~60%) are Fe free and about 11% cells contain one Fe atom. The simulated small system contains a total of 85 Fe atoms, so we can think of each cell having 1.33 Fe atom on average. The cells which are more than half-filled ($n > 4$) are present in significant proportions, adding up to 13%. The Fe atoms thus seem to have depleted from a large part of the supercell and clumped in small areas of the supercell. The Mg-cell frequency takes the largest value for the two-atom count, which is close to the average count of 1.64 Mg per cell. The Si-cell frequency distribution is relatively narrow with a peak at one-atom count which is close to the average per-cell count of 1.13 Si. Around 20% of cells are free of either Mg or Si, and these depleted atoms unlike Fe atoms do not pile up in a few cells because the $n > 4$ cell frequency is almost zero for either species. Finally, the O-cell frequency shows a near-normal distribution with a small zero-atom occurrence (~3%) and a broad peak between $n = 4$ and 5, which is consistent with the average per-cell count of 3.92 O.

We perform the binning analysis for the DPMD position-time series obtained from the simulations of small and large supercells. The calculated cell frequency distributions of all elements for the 512-atom supercell essentially overlap with the corresponding FPMD distributions thereby justifying a good accuracy of the deep potential used in our simulation (Supplementary Fig. S7). The large 32768-atom DPMD supercell is divided into the 16×16×16 mesh. As such, the number of cells/bins is large (4096 cells) compared to 64 cells of the small supercell though the bin size remains the same (4.25 Å wide). The difference in the number of the bins produces notable changes in the cell frequency distributions of different elements (Fig. 5, center). In particular, the Fe-cell frequency shows a clear bump at the 6-atom count, and both Mg and O frequencies show a depression after the zero-atom count before they start to increase with increasing n. The other features, including the peak positions and amplitudes generally agree between the DPMD and FPMD results. For the large DPMD supercell, we also consider the 8×8×8 decomposition which results in 512 cells (Supplementary Fig. S8). The cubic bin is 8.5 Å wide and contains an average of 64 atoms. The calculated cell frequency distributions of four elements

(Fig. 5, right) differ considerably from those obtained using the small bin size (Fig. 5, center). Interestingly, the bimodal features of all elemental distributions are dramatically enhanced when the binning is done with the coarse mesh (that is, using the large bin). The peak at or near zero-atom count and the peak at high-atom count are clearly separated from each other in all three distributions, and all peaks are well defined and clearly identifiable.

The Fe cell frequency takes highest value (~ 45%) at the zero-atom count and shows a clear peak around $n = 54$ (Fig. 5, right). The Mg cell frequency is high (~11 %) at $n = 0$ and shows a clear peak $n = 16$. Both Si and O frequencies take a finite value of 5% at $n = 0$ and then show a peak at $n = 10$ and 38, respectively. We thus find that the spatial distribution of Fe atoms differs considerably from the distributions of other two cations even though these elements are present in the simulated system in similar proportions. First, the Fe-free cells are much more abundant than either Mg-free cells or Si-free cells based on the binning analyses of both small and large supercells. Second, the high atom-count cells (with $n > 5$ for the small system or $n > 40$ for the large system) are present in significant proportions for Fe but not for Mg and Si.

It is important to understand how the under-occupied cells and over-occupied cells with respect to different atomic species are spatially related. We explore this relation with respect to the Fe-cell occupancy by calculating the separate numbers of each element that are associated with the cells designated by Fe-atom count (n_{Fe}) for the DPMD supercell using the large bins (Fig. 6). For instance, the spatial distribution of magnesium represents how the number of Mg atoms that are collectively present in all cells of given Fe-atom count varies with n_{Fe}. The calculated Fe distribution shows a broad peak centered at the 54-atom count, and most Fe atoms (~75%) contribute to the cells which are more than half filled with Fe. The remaining Fe gets dispersed in other parts, including cells covered by the first peak ($n_{Fe} = 0$ to 6). Interestingly, these Fe-poor cells contribute to the primary peaks of the other three elemental distributions. The spatial distributions of Mg, Si, and O each shows a high value at $n_{Fe} = 0$ and then rapidly decreases with increasing n_{Fe}. This means that these elements are mostly contained in the Fe-poor cells. A small fraction of Mg atoms (~1%) resides in the cells with $n_{Fe} > 32$ thus implying that Fe and Mg tend to avoid each other. Fe atoms also avoid Si and O atoms to lesser extents, and ~5% Si and ~3% O atoms are present in those Fe-rich cells.

The predicted inhomogeneous spatial distributions of four elements in the simulated supercell broadly correspond to two types of cells. There are the cells defining the parts of the supercell which are enriched in Fe but depleted in other elements and there are also the parts which are enriched in Mg, Si and O but depleted in Fe. A chemical segregation can be implied only if the cells of each type are contiguous in the space. The visualization and adjacency check suggest that the Fe-rich cells tend to remain connected in one or more directions and thus may collectively form one Fe-rich domain of the supercell. Similarly, the Fe-poor cells appear to be contiguous in the space thereby forming another domain which is rich in Mg, Si, and O. The two domains may be separated by the third type of cells with moderate Fe contents corresponding to the wide gap between the two peaks in the spatial distributions of Fe atoms (Fig. 6).

Composition evaluation. The structural and spatial analyses of the atomic position-time series suggest that the simulated bulk earth melt system undergoes a chemical differentiation into two phases. One of them is rich in Fe and may contain other elements in small amounts. This region is referred to as the metallic phase. The other region which is mostly composed of Mg, Si, and O containing Fe in small amount corresponds to the magma ocean phase. To accurately determine the composition of each phase in terms of the proportions of the four elements present in the melt system, we identify the cells that make up the corresponding domain in the large supercell configurations produced by DPMD simulations. This requires the use of appropriate threshold on the number of the atoms of a given type that reside in a cell based on the spatial distribution functions (Fig. 6). We consider the cells that contain 44 or more Fe atoms corresponding to the second peak of the Fe distribution function to be part of the metallic domain. These cells are more than half filled with Fe and their contents are much higher than the average value of 10.6 Fe per cell. The $n_{Fe} \geq 44$ range also includes the shallow bumps in both the Si and O distributions (Fig 6, inset). On the other hand, the magma ocean domain is anticipated to be a mixture of silicate and oxide. To infer its composition, we can safely consider all cells with $n_{Fe} = 0$ as they contain Mg, Si, and O atoms in high abundances. The composition is expected to incorporate some Fe as well. The cells for $n_{Fe} \leq 6$ correspond to the first peak of the Fe distribution and they also cover the major peak of each other elemental distribution (Fig 6, inset). As such, these Fe-poor cells are taken to be part of the magma ocean domain.

The cells with $n_{Fe} \geq 44$ incorporate a total of 61% Fe atoms to form the metallic domain. By counting the other atomic species in these Fe-rich cells, we associate 2.8% Si, 1.3% O, and 0.16% Mg with this domain. When the elemental proportions are expressed in weight percent, the composition of the metallic domain consists of 96.2, 0.14, 1.9, and 1.7 wt% of Fe, Mg, Si, and O, respectively (Table 1). The cells with $n_{Fe} \leq 6$ are depleted in Fe and incorporate 4.9% iron. These cells collectively contain Mg, Si, and O in large proportions of 90.1, 83.3, and 86.6%, respectively. The magma ocean phase is thus composed of 3.0 wt% Fe, 29.7 wt% Mg, 22.0 wt% Si, and 45.3 wt% O. For each atomic species, the abundances of the atoms that are included to the metallic liquid and magma ocean domains do not add up to 100%. Around one-third Fe and smaller proportions (15 to 20%) of Mg, Si, and O do not belong to either phase. These unassigned atoms mostly form the boundary/interface between the small Fe-rich cluster and the surrounding Fe-poor magma ocean region. They may also form a few small pocket areas that are not considered to be part of the magma ocean domain.

It is important to demonstrate that the results for the metallic and magma ocean compositions evaluated using the 3D binning method are robust for the size of bins/cells and the iron-atom (n_{Fe}) cutoffs used to characterize the segregated phases. The Fe atom distribution shows a bimodal feature for four other meshes 16×16×16, 14×14×14, 12×12×12, and 10×10×10 (Supplementary Fig. S9) besides the 8×8×8 mesh considered for the analysis (Fig. 6). For each binning mesh, the first peak corresponds to the magma ocean and the second peak corresponds to the metal. With

increasing size of bins (that is, with coarser mesh), the gap between the two peaks widens and as such, it becomes easier to choose appropriate n_{Fe} cutoffs for defining the phase separation. It is remarkable that the inferred compositions do not differ substantially among the five binning cases (Supplementary Table S1). However, the effects of changing cutoff are large for the 16×16×16 mesh using the small bins (4.25 Å wide, 8 atoms per bin). The cutoff effects are systematically suppressed with coarser meshes and become considerably small for the 8×8×8 mesh with 8.5 Å wide bins and 64 atoms per bin (Supplementary Table S1).

We now examine how the predicted spatial segregation of four elements in the simulated supercell is sensitive to temperature. In particular, the spatial distribution of Fe atoms defined with respect to the Fe-atom cell count (n_{Fe}) at 3500 and 4000 K differs considerably from the distribution at 3000 K (Fig. 7). As temperature increases, the first peak gets taller and is shifted to the right whereas the second peak is shifted to the left. The cells that are associated with the magma ocean domain gain more Fe atoms as the iron-rich cells lose their Fe atoms. The spatial distributions of other three elements show the temperature-induced changes in an opposite way. The first peak gets shorter and extends to the right for each distribution and the second bump-like feature gets enhanced for both Si and O distributions (Supplementary Fig. S10). The cells forming the metallic domain gain more Si and O as all elements become more mobile and are redistributed at higher temperature. Our finding that the spatial distributions of four elements each shows two identifiable peaks which are separated by a large n_{Fe} gap (Fig. 7) thus implies a chemical phase segregation at the elevated temperatures. To infer the composition of the magma ocean, the cells with $n_{Fe} \leq 7$ and $n_{Fe} \leq 8$ are considered at 3500 and 4000 K, respectively. For the metal, we adopt respective thresholds of $n_{Fe} \geq 38$ and $n_{Fe} \geq 32$. The inferred compositions of the segregated phases are found to be sensitive to temperature (Table 1). As temperature is increased, the metallic region gains Si and O by a factor of 4 between 3000 and 4000 K. Over the same temperature interval, the Fe content of the magma ocean region increases three times. This means that temperature tends to promote the mixing between the metal and silicate/oxide liquids.

Table 1: Major element compositions (in weight percents) of the metallic and magma ocean phases of simulated melt system at three different conditions compared with the bulk Earth model compositions[23,31]. Uncertainties estimated using the block averaging method are given in parentheses for the last digits reported.

	3000 K 29.1 (2) GPa	3500 K 32.1 (3) GPa	4000 K 35.0 (5) GPa	Bulk earth model
	Metal			Core
Fe (wt%)	96.2 (8)	89.1 (6)	81.8 (14)	95.5
Mg (wt%)	0.14 (1)	0.61 (22)	2.4 (3)	0.0
Si (wt%)	1.9 (6)	5.8 (4)	8.7 (15)	3.0
O (wt%)	1.7 (2)	4.6 (2)	7.1 (2)	1.5
	Magma ocean			Mantle
Fe (wt.%)	3.0 (5)	5.5 (4)	9.0 (5)	6.9
Mg (wt.%)	29.7 (1)	29.7 (3)	28.8 (2)	28.0
Si (wt.%)	22.0 (3)	20.6 (4)	19.3 (6)	21.0
O (wt.%)	45.3 (2)	44.3 (2)	42.9 (2)	44.0

Discussion and implications

The predicted compositions of the metallic and magma ocean phases can be further understood in terms of the local coordination environments. In the metallic domain, Fe or any other element is expected to be highly coordinated with iron atoms[28]. Over 80% Fe atoms in the simulated large supercell is associated with the nine-fold or higher coordination states. Interestingly, 3.7% Si is coordinated with nine or more Fe atoms. Such Si is less likely to form bonds with O; we find that 3.4% Si is not coordinated with O. In contrast, Mg shows weak coordination with Fe and is thus less likely to exist in the Fe-rich region. Not all O is bonded with Mg and/or Si. Such O if present in the Fe-rich region is expected to be well coordinated with Fe but to a lesser extent compared to other elements; we find that 1.2% O is bonded with five or more Fe atoms.

Fe atoms which are undercoordinated with other Fe atoms (thus existing as isolated single atom or pair or triplet) are likely to be well coordinated with O to form polyhedral units. Such Fe atoms present in about 2.8% can be associated with the magma ocean. This region also includes Si and O atoms which are not coordinated with Fe in high proportions (~80 and ~88%, respectively). Unlike the other two cations, Mg is exclusively bonded with O thereby forming polyhedral units. The predicted elemental proportions of both magma ocean and metallic phases thus appear to be consistent with the coordination statistics.

As discussed earlier, the structural and space-decomposition analyses of the 512-atom supercell used in the FPMD simulation suggest a chemical phase separation (Fig. 1). An important question is whether reasonable compositional estimate can be made for the segregated liquid phases by using the spatial distributions of four elements defined with respect to the Fe-atom cell count (n_{Fe}) in the range 0 to 8 (Supplementary Fig. S7). We consider the cells with $n_{Fe} \geq 5$ for the metal and the cells with $n_{Fe} \leq 1$ for the magma ocean at 3000 K, seemingly consistent with the respective thresholds of $n_{Fe} \geq 44$ and $n_{Fe} \leq 6$ used for the large supercell. The inferred composition comprises more Mg (0.8 wt%) and O (4.8 wt%) for the metal and more Fe (5.8 wt%) for the magma ocean compared to the corresponding compositions evaluated earlier for the large system (Table 1). Visualization of the atomic configurations reveals that the Mg and O atoms that are included in the Fe-rich cells tend to reside in the outer parts of the metallic region (Supplementary Fig. S5). It is not clear that to what extent these atoms should be counted in evaluating the composition of the metallic phase.

We compare our simulation results for the metal and silicate compositions with those derived from experimental data in Fig. 8. Experimental predictions are derived using the mass balance approach[4] coupled with the partitioning expressions[13] for Si and O and assuming ideal solution behavior. We calculate the distribution of Mg between metal and silicate using the exchange reaction parameterization[29] following the prediction of Mg, Si, and O distributions. Both our DPMD predictions and those from experiment consider the reaction of the same bulk composition at equal pressure and temperature conditions. We also evaluate the oxygen fugacity relative to the iron-wüsite (IW) oxygen buffer using $\Delta IW = 2\log\left(\frac{x_{FeO}}{x_{Fe}}\right)$, where x_{FeO} is the molar fraction of FeO in the magma ocean phase and x_{Fe} is the molar fraction of Fe in the metallic phase. The results suggest that our simulations represent reduced condition with oxygen fugacity lying 3.1 to 1.8 log units below IW at 3000 to 4000 K (Supplementary Table S2).

Our prediction that Mg, Si, and O increasingly dissolve into liquid iron under higher temperatures is consistent with the experimental inferences (Fig. 8). The net effect of Si and O dissolution into metal is oxidation, as manifested by the rise in FeO concentration in the magma ocean with temperature, in both our DPMD predictions and those from experimental works. The predicted Si concentrations of metal match well between the two approaches while our predicted O concentrations are about twice that compared to experimental values. The retention of O in the metal, as opposed to the magma ocean, make our predicted oxygen fugacities (quantified as deviations from the IW buffer) somewhat more reduced than those inferred from the experiments[30] although the difference between the two methods remains less than one log unit (Supplementary Table S2). Our predicted Mg concentrations remain remarkably like experimental values for the 3000 and 3500 K scenarios while our predicted Mg concentrations in metal exceed experimental value at 4000 K by ~ 2 wt%. The overall correspondence between the simulation results and experimentally inferred values gives confidence that DPMD can accurately predict elemental distributions in high pressure, temperature systems that are difficult to study via experiment.

A chemical phase separation of the bulk earth melt system can be viewed as a precursor to the core-mantle formation. Such phase separation could have occurred in early history thereby setting a path for the subsequent chemical evolution leading to the final compositions of the mantle and core[31]. It is remarkable that the predicted compositions of the magma ocean and metallic liquid (Table 1) are generally consistent with the compositions of the today's mantle and core, respectively[4,23,31]. Establishing a two liquid phase model for the bulk composition of the earth as we demonstrate in the study is important to investigate further details of the chemical and physical processes driving the core-mantle differentiation. This model allows us to study the incorporation of other elements besides those four elements considered in the present simulations to infer more realistic compositions[16]. The partitioning coefficients of volatile elements and other trace elements can be evaluated from such two-phase simulations. Improved knowledge about the composition and elemental partitioning is not only important to explain the geophysical and geochemical observations but also understand the process and timing of the core formation.

Methods

First-principles molecular dynamics (FPMD) simulations were performed within the generalized gradients approximation (GGA) and projector augmented wave formalism using VASP - Vienna ab initio simulation package[17]. The GGA functional used was Perdew-Burke-Ernzerhof type as in most previous computational studies[32]. The gamma point was used for the Brillouin zone sampling and the energy cutoff of 600 eV was used for the plane wave basis set. Because of high computational cost, FPMD can handle relatively small system and generate relatively short runs. Therefore, we also used the neural network-based approach, which is much faster than the first-principles approach. A deep neural network model was trained with the first-principles energy and force data to generate many-body potential and interatomic force field[33,34]. The corresponding simulations are referred to as deep potential molecular dynamics (DPMD).

The supercell used in the FPMD simulations consists of 512 atoms for a mixed metal-magma ocean system that represents a major-element bulk earth composition of $Fe_{85}Mg_{104}Si_{72}O_{251}$. The model thus consists of Fe, Mg, Si, and O in the amounts of 35.7, 19.0, 15.2, and 30.2 wt%, respectively. For our starting composition, the O/Si and FeO/Fe weight ratios are 1.99 and 0.047, respectively, which make the oxidation of our simulations comparable to that of the bulk Earth compositional model[23,31]. Our simulations were based on the canonical *N*-*V*-*T* ensemble with Nose thermostat, where *N* is the number of atoms, *V* is the volume, and *T* is the temperature. The initial liquid configuration was created and thermalized at 6000 K for the $Mg_{189}Si_{72}O_{251}$ system. Then 85 Mg atoms were replaced by iron atoms and the supercell was again thermalized at 6000 K by performing FPMD simulations for 20 picoseconds using a time step of 1femtosecond (Supplementary Fig. S1). The configuration was then quenched down to the desired lower temperatures of 4000 K, 3500, and 3000 K and simulation runs were performed for 20 to 50 picoseconds. At each thermodynamic state considered, the total pressure represents the sum of the pressure obtained from the simulation, the ideal gas contribution given by NkT/V (where k is

Boltzmann constant). We used the atomic-position time series to analyze the local structure and speciation and to identify the segregated phases and estimate their compositions.

A deep neural network potential model was constructed for bulk earth melt system by training the first-principles data at three different temperatures using the DeePMD-kit package[33]. The corresponding snapshots/configurations from the FPMD trajectories were split 80 and 20% for training and validation, respectively. Each configuration was labelled with energy and forces. We used the embedding neural network with a size of (25, 50, 100) to convert the atomic local environment to a descriptor and a fitting neural network with a size of (240, 240, 240) to transfer the descriptor into atomic energy. The start learning rate, decay steps, and the end learning rate were set to 0.001, 2000, and 3.51×10^{-8}. The pre-factors of the loss function were allowed to increase from 0.02 to 1.0 for energy and to decrease from 1000 to 1 for force. The potential was trained using a stochastic gradient descent approach, which we ran for one million steps. The trained deep potential model was then used to perform molecular dynamics simulations using the LAMMPS package[35]. The accuracy of the deep-learning potential was first confirmed by comparing the predicted energy, forces, and pressures with those from the first-principles approach (Supplementary Fig. S11).

The 512-atom configuration from the FPMD run at 4000 K was repeated four times along each direction to create the 32768-atom supercell corresponding to the $Fe_{5440}Mg_{6656}Si_{4608}O_{16064}$ composition (Fig. 1, bottom). This large supercell was used to run the DPMD simulation at 4000 K for 2 nanoseconds with a time step of 1 femtosecond. As discussed later, the melt system underwent a phase separation. The 4000 K configuration was then quenched down to 3500 and 3000 K and long DPMD runs of 1 nanosecond was performed to show that the chemical phase segregation becomes more pronounced at lower temperature. The output position-time series data were analyzed to characterize the segregated phases geometrically and compositionally.

References

1. Canup, R. M., 2008. Accretion of the Earth. *Phil. Trans. Roy. Soc. A* **366**, 4061-4075.
2. Elkins-Tanton, L. T., 2012. Magma oceans in the inner solar system, *An. Rev. Earth Planet. Sci.* **40**, 113-139.
3. Wood, B. J., Walter, M. J., Wade, J., 2006. Accretion of the Earth and segregation of its core. *Nature* **441**, 825-833.
4. Rubie, D. C., Frost, D. J., Mann, U., Asahara, Y., Nimmo, F., Tsuno, K., Kegler, P., Holzheid, A., and Palme, H., 2011. Heterogeneous accretion, composition and core–mantle differentiation of the Earth. *Earth Planet. Sci. Lett.* **301**, 31–42.
5. Rubie, D. C., Melosh, H. J., Reid, J. E., Liebske, C. and Righter, K., 2003. Mechanisms of metal–silicate equilibration in the terrestrial magma ocean. *Earth Planet. Sci. Lett.* **205**, 239-255.
6. Rudge, J. F., Kleine, T., Bourdon, B., 2010. Broad bounds on Earth's accretion and core formation constrained by geochemical models. *Nat. Geosci.* **3**, 439–443.

7. Xiong, Z., Tsuchiya, T., Van Orman, J. A., 2021. Helium and argon partitioning between liquid iron and silicate melt at high pressure. *Geophys. Res. Lett.* **48**, e2020GL090769.
8. Zipfel, J., Palme, H., Kennedy, A., Hutcheon, I., 1995. Chemical composition and origin of the Acapulco meteorite. *Geochim. Cosmochim. Acta* **59**, 3607–3627.
9. Chambers, J., 2006. Meteoritic diversity and planetesimal formation. In Meteorites and the Early Solar System II, *University of Arizona Press*, 487-497.
10. Terasaki, H., Frost, D. J., Rubie, D. C., Langenhorst, F., 2007. Interconnectivity of Fe-O-S liquid in polycrystalline silicate perovskite at lower mantle conditions. *Phys. Earth Planet. Inter.* **161**, 170–176.
11. Berg, M. T. L., Bromiley, G. D., Le Godec, Y., Philippe, J., Mezouar, M., Perrillat, J. -P., Potts, N. J., 2018. Rapid core formation in terrestrial planets by percolative flow: In-situ imaging of metallic melt migration under high pressure/temperature conditions. *Front. Earth Sci*. **6**, 77.
12. Siebert, J., Badro, J. D. Antonangeli, D., Ryerson, F. J., 2012. Metal–silicate partitioning of Ni and Co in a deep magma ocean. *Earth Planet. Sci. Lett.* **321**, 189–197.
13. Fischer, R. A., Nakajima, Y., Campbell, A. J., Frost, D. J., Harries, D., Langenhorst, F., Miyajima, N., Pollok, K., Rubie, D. C., 2015. High pressure metal–silicate partitioning of Ni, Co, V, Cr, Si, and O. *Geochim. Cosmochim. Acta* **167**, 177–194.
14. Hirose, K., Wood, B. Vočadlo, L., 2021. Light elements in the Earth's core. *Nat. Rev. Earth Environ.* **2**, 645–658.
15. Zhang, Y., Guo G. 2009. Partitioning of Si and O between liquid iron and silicate melt: A two-phase ab-initio molecular dynamics study. *Geophys. Res. Lett.* **36**, 18305.
16. Zhang, Y., Yin Q. Z., 2012. Carbon and other light element contents in the Earth's core based on first-principles molecular dynamics. *Proc. Nat. Acad. Sci.* **109**, 19579-19583.
17. Kresse, G., Furthmüller, J., 1996. Efficient iterative schemes for ab initio total-energy calculations using a plane-wave basis set. *Phys. Rev. B* **54**, 11169–11186.
18. Zhang, L., Han, J., Wang, H., Car, R., Weinan, E., 2018. Deep Potential Molecular Dynamics: A Scalable Model with the Accuracy of Quantum Mechanics. *Phys. Rev. Lett.* **120**, 143001.
19. Luo, H., Karki, B. B., Ghosh, D. B., Bao, H., 2021. Deep neural network potentials for diffusional lithium isotope fractionation in silicate melts. *Geochim. Cosmochim. Acta* **303**, 38–50.
20. Wen, T. Zhang, L., Wang, H., Weinan, E., Srolovitz, D.J., 2022. Deep potentials for materials science. Mater. *Futures* **1**, 022601.
21. Wang, K. Lu, X., Liu, X., Yin, K., 2023. Noble gas (He, Ne, and Ar) solubilities in high-pressure silicate melts calculated based on deep-potential modeling. *Geochim. Cosmochim. Acta* **350**, 57–68.
22. Xu, F. Y., Li, G. Z., Chen, X. R., Geng, H. Y., Liu, L., Hu, J., 2024. Probing the critical point of $MgSiO_3$ using deep potential simulation. *J. Appl. Phys.* **135**, 125901.
23. McDonough, W. F., Sun, S. S., 1995. The composition of the Earth. *Chem. Geol.* **120**, 223-253.
24. Wood, B. J., 2008. Accretion and core formation: Constraints from metal-silicate partitioning. *Philos. Trans. R. Soc., Ser.* A **366**, 4339-4355.
25. Ghosh, D. B. and Karki, B. B., 2016. Solid-liquid density and spin crossovers in (Mg, Fe) O system at deep mantle conditions. *Sci. Rep*. **6**, 37269.
26. Ghosh, D. B. and Karki, B. B., 2020. Effects of valence and spin of Fe in $MgSiO_3$ melts: Structural insights from first-principles molecular dynamics simulations. *Geochim. Cosmochim. Acta* **279**, 107-118.
27. Bhattarai, D. and Karki, B. B, 2009. Atomistic visualization: space–time multiresolution integration of data analysis and rendering. *J Mol Graph Model* **27**, 951–968.

28. Alfe, D., Kresse, G., Gillan, M. J., 2000. Structure and dynamics of liquid iron under Earth's core conditions. *Phys. Rev. B* **61**, 132–142.
29. Badro, J., Aubert, J., Hirose, K., Nomura, R., Blanchard, I., Borensztajn, S, Siebert, J., 2018. Magnesium partitioning between Earth's mantle and core and its potential to drive an early exsolution geodynamo. *Geophys. Res. Lett*. **45**, 13,240-13,248.
30. Corgne, A., Keshav, S., Wood, B. J., McDonough, W. F., Fei, Y., 2008. Metal-silicate partitioning and constraints on core composition and oxygen fugacity during earth accretion, *Geochim. Cosmochim. Acta* **72**, 574– 589.
31. McDonough, W. F., 2003. Compositional model for the Earth's core, in *The Mantle and Core, Treatise Geochem*, **2**, edited by R. W.Carlson, Elsevier-Pergamon, Oxford, U. K.
32. Perdew, J. P., Burke, K., Ernzerhof, M., 1996. Generalized gradient approximation made simple. *Phys. Rev. Lett*. **77**, 3865–3868.
33. Wang, H., Zhang, L., Han, J., Weinan, E., 2018. DeePMD-kit: A deep learning package for many-body potential energy representation and molecular dynamics. *Comput. Phys. Commun.* **228**, 178–184.
34. Zhang, Y., Haidi, W., Chen, W., Zeng, J., Zhang, L., Wang, H., Weinan, E., 2020. DPGEN: A concurrent learning platform for the generation of reliable deep learning-based potential energy models. *Comput. Phys. Commun.* **253**, 107206.
35. Thompson, A. P. et al., "LAMMPS Molecular Dynamics Simulator, Comp Phys Comm. [Online]. Available https://www.lammps.org/

Acknowledgements

The research was supported by NASA (80NSSC21K0377) and NSF (EAR 1463807). The computing resources were provided by Louisiana State University High Performance Computing.

Author contributions

A.S. and B.B.K. performed simulations and analyzed the results. All authors contributed to the analysis and discussion of the results, and to the preparation of the manuscript.

Competing interests

The authors declare no competing interests.

Additional information

Supplementary Information: The online version contains supplementary figures.

Correspondence and requests for materials should be addressed to B.B.K.

Data availability

All data generated or analyzed during this study are included in this published article and its supplementary information file.

Figures and Figure Captions

Figure 1. Visualization snapshots of simulated melt systems. The initial configuration of the 512-atom melt system was equilibrated at 6000 K and 49.4 GPa with FPMD and then subsequently quenched to 3000 K and 29.1 GPa. The gold, green, and blue spheres represent 85 Fe, 104 Mg, and 72 Si atoms, respectively, whereas the small red spheres represent 251 O atoms. The equilibrated snapshot at 3000 K is shown for the large supercell consisting of total 32768 atoms simulated with DPMD. For the sake of clarity, all atoms are translated so that the iron clustered region appears at the center of the front face of the supercells.

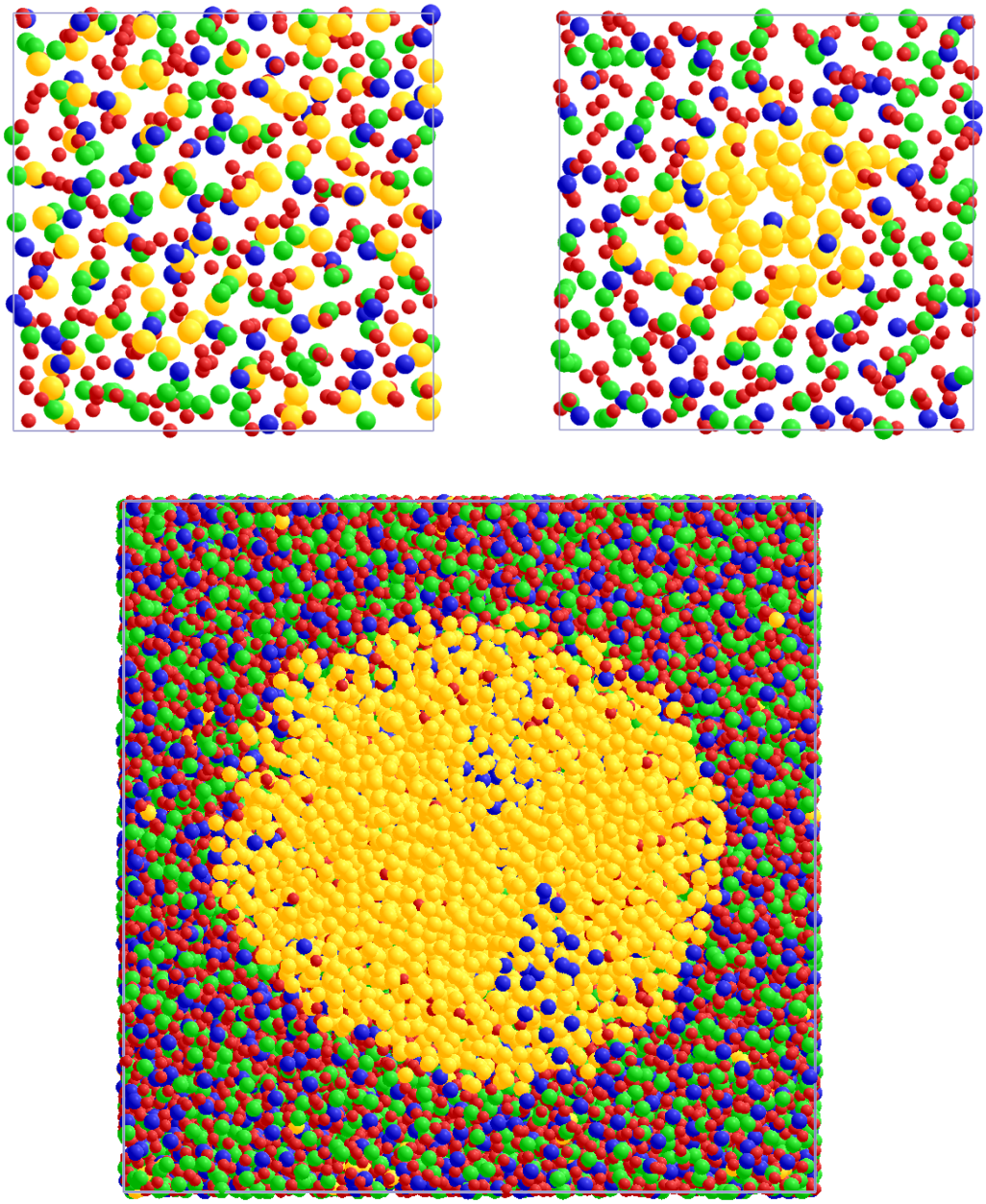

Figure 2. Partial radial distribution functions (RDFs) for simulated melt systems. All cation-anion pairs (left) and all cation-cation pairs (right) at 3000 K and 29.1 GPa are from the FPMD simulation of the small system (also shown is the oxygen-oxygen function). The FeO, FeFe, and FeSi functions from the DPMD simulation of the large system at the same condition are shown (dotted curves).

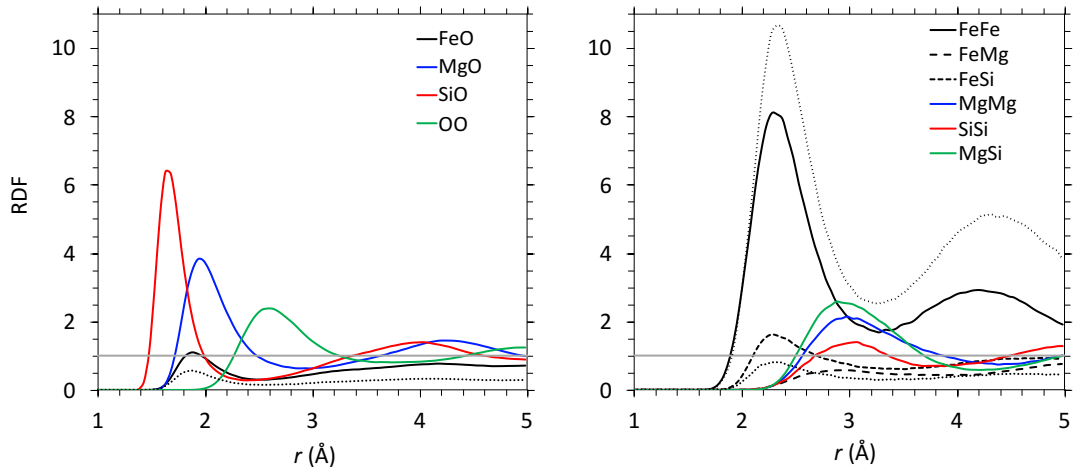

Figure 3. Coordination distributions of simulated melt systems. Selected coordination types at 3000 K and 29.1 GPa from the FPMD simulation of the small system (solid lines with filled symbols) are compared with the corresponding DPMD results for the large system at the same conditions (dashed lines with open symbols).

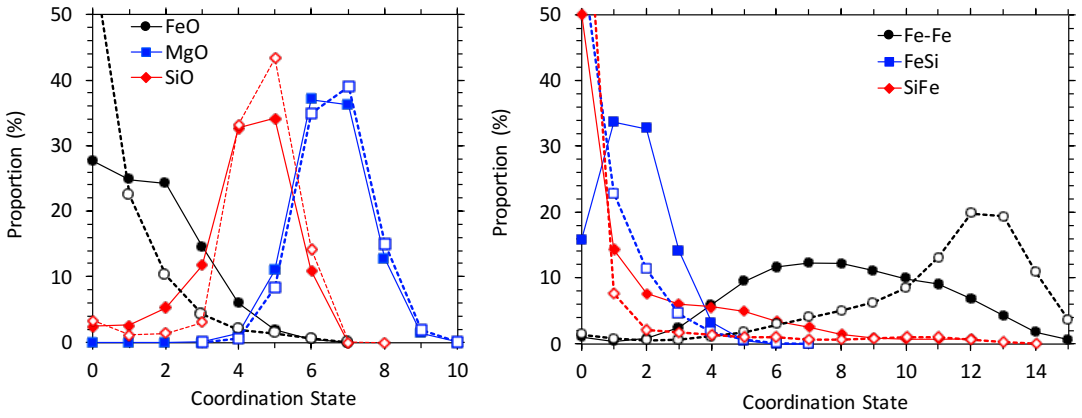

Figure 4. Visualization snapshots of the Fe-Fe and Fe-O coordination environments in the simulated melt systems. The numbers of the bonds emanating from gold spheres (iron atoms) represent different Fe-Fe coordination states; each iron atom is coordinated with three or more iron atoms (top-left). Gold spheres with no links with red spheres represent the iron atoms which are not bonded with oxygen (top-bottom). Other iron atoms are singly, doubly, and triply coordinated with oxygen except two four-fold (tetrahedral) coordination states. In the large system (bottom), Fe-O coordination polyhedra are present in the surrounding region.

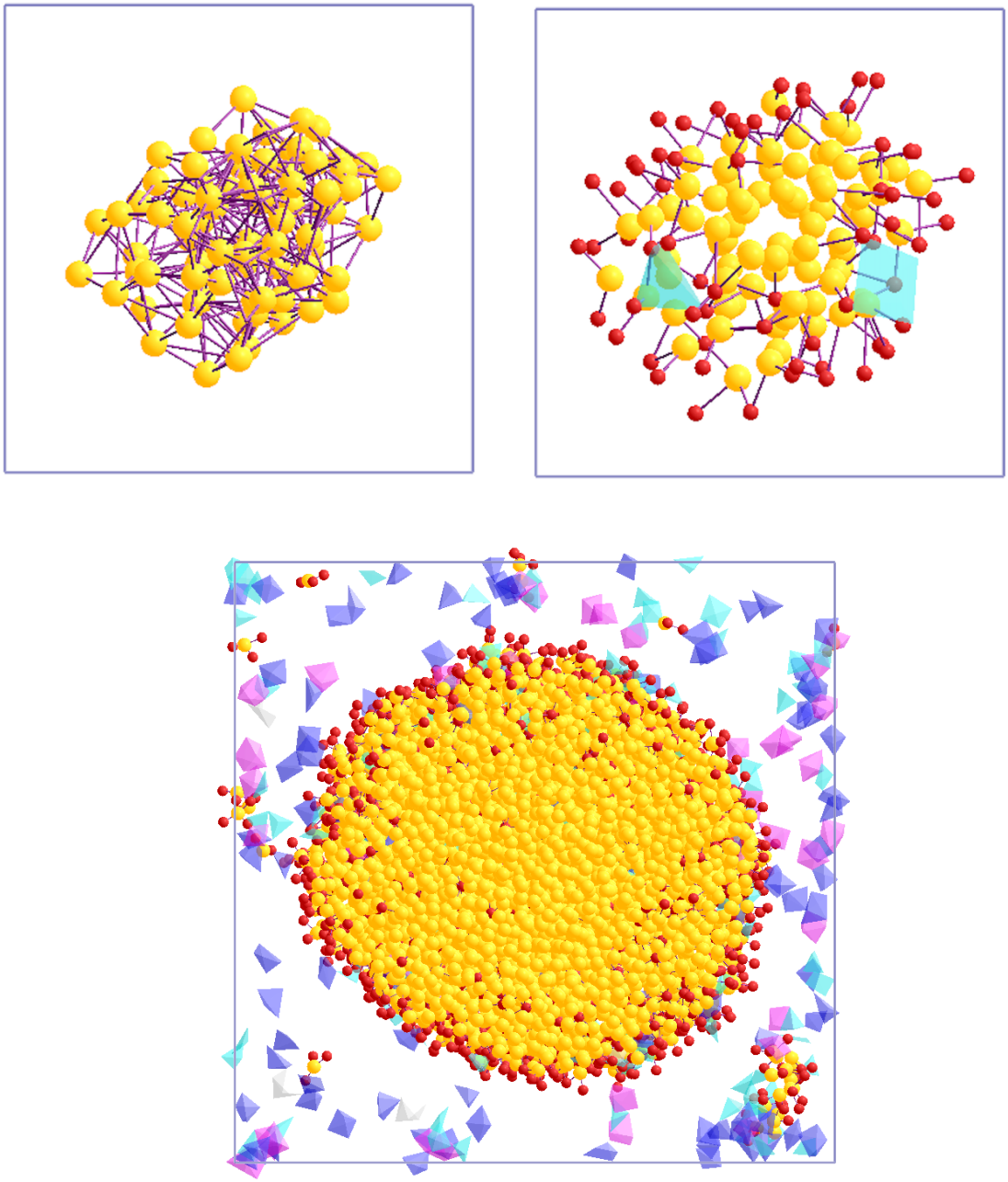

Figure 5. Cell frequency distributions at 3000 K and 29.1 GPa. The cell frequency versus the per-cell atom count (n) of Fe, Mg, Si, and O in the small system simulated with FPMD (left) is compared with the corresponding results for the large system simulated with DPMD (center and right). The inset compares the iron frequency distribution (f) between FPMD (solid circles) and DPMD (open circles).

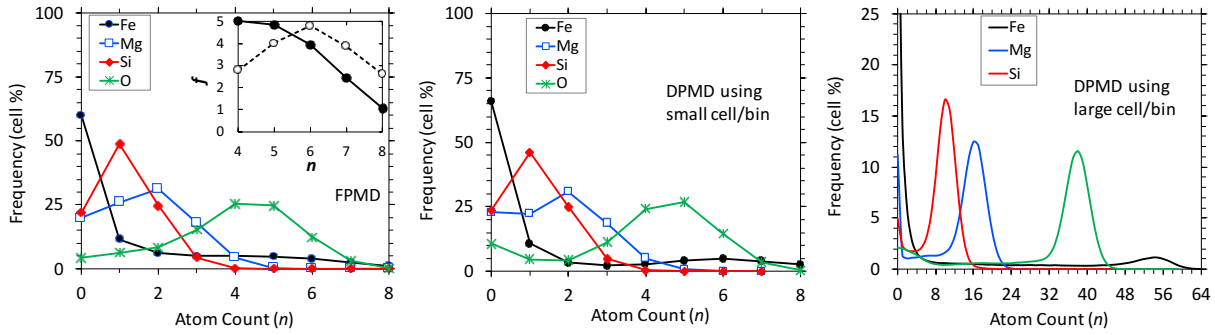

Figure 6. Elemental distributions in the large supercell. Spatial distribution of each element is calculated with respect to the iron-atom count per cell (n_{Fe}) for large DPMD supercell configurations at 3000 K and ~30 GPa. The inset magnifies low atom count range and marks thresholds for iron-poor and iron-rich cells (dotted vertical lines).

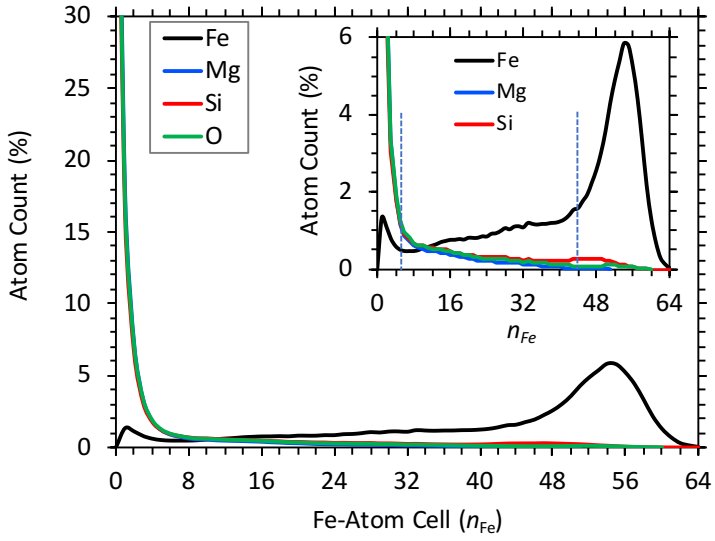

Figure 7. Temperature effects on spatial distribution of iron. For the large melt system simulated with DPMD, the calculated iron distribution with respect to the iron-atom count per cell (n_{Fe}) is shown at three different temperatures (29.1 to 35.0 GPa).

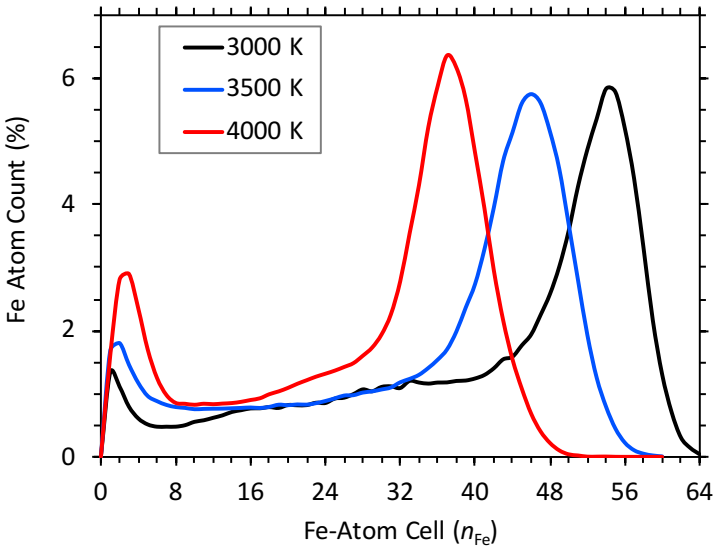

Figure 8. Comparisons between the predicted and experimentally inferred compositions. The weight percents of three oxides are plotted for the silicate magma ocean (upper panel) and the weight percents of four elements are plotted for the metallic phase (lower panel). For each phase, the simulation results are shown by solid lines with symbols and the experiment-based results[4,13,29] are shown by dashed lines. The amount of Fe is divided by 10 to display its curves (black lines).